ACS APPLIED NANO MATERIALS
Cite This: ACS Appl. Nano Mater. 2018, 1, 2997−3005
Article
www.acsanm.org

Three-Dimensional Carbon Nanotube/Transition-Metal Oxide Sponges as Composite Electrodes with Enhanced Electrochemical Performance

Yufeng Luo,[†,‡] Ke Wang,[†] Shu Luo,[†,‡] Fei Zhao,[†] Hengcai Wu,[†] Kaili Jiang,[†,§] Qunqing Li,[†,§] Shoushan Fan,[†,‡] and Jiaping Wang*[,†,§]

[†]Department of Physics and Tsinghua-Foxconn Nanotechnology Research Center, Tsinghua University, Beijing 100084, China
[‡]School of Materials Science and Engineering, Tsinghua University, Beijing 100084, China
[§]Collaborative Innovation Center of Quantum Matter, Beijing 100084, China

Supporting Information

ABSTRACT: Innovative three-dimensional (3D) carbon nanotube (CNT)/transition-metal oxide (TMO) sponge electrodes are synthesized by freeze-drying and calcination processes. The high specific surface area and porosity of the CNT sponge provide more attachment sites for the TMO nanoparticles, a larger contact area with electrolytes, and more space for volume expansion, which enable the CNT/TMO sponge electrodes to exhibit ultrahigh reversible capacity and excellent cycling stability. The continuous CNT network in this new type of electrode can fully satisfy fast electron-transfer kinetics; thus, excellent rate performance is realized. Furthermore, the unique structural characteristics of the 3D CNT sponge make it suitable for making almost all kinds of CNT/TMO composite electrodes, reflecting its versatility for use in many battery systems.

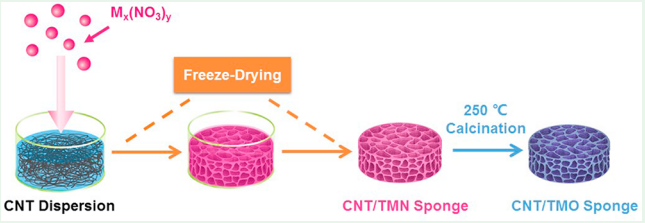

KEYWORDS: *carbon nanotube sponge, transition-metal oxide, composite electrode, three-dimensional structure, lithium-ion battery*

1. INTRODUCTION

Recently, transition-metal oxides (TMOs), such as MnO_2,[1−10] NiO,[11−13] Fe_2O_3,[14−16] and Co_3O_4,[17−19] have attracted widespread attention for their application in lithium-ion batteries (LIBs) because of their high theoretical specific capacity, environmental friendliness, and natural abundance. TMOs are generally considered to be ideal alternatives to graphite anodes (~372 mA h g^{-1}) because it has become more difficult for graphite anodes to meet the increasing market demand for high energy and power density. However, there are still two major drawbacks that hinder the practical application of the TMO electrodes. The first drawback is the severe degradation caused by volumetric expansion during the discharge and charge processes. The second drawback is the low intrinsic electrical conductivity of TMOs, which seriously hinders the reaction activity. Some strategies have been proposed to address these drawbacks. The fabrication of different nanostructures, such as nanosheets,[8] nanorods,[12,16] and hollow structures,[3,5,7,11,20] is beneficial for rapid lithium-ion diffusion because of their high reaction areas. The employment of carbonaceous materials, such as carbon nanofibers,[10,21−23] carbon nanotubes (CNTs),[1] graphene,[9,19] and reduced graphene oxide (rGO),[2,6,14,24] has also been proposed owing to their high conductivity and excellent ductility. Among these structures, three-dimensional (3D) carbonaceous materials can effectively accommodate the volumetric expansion during the discharge/change processes and simultaneously enhance the reaction kinetics.

3D composite electrodes have attracted widespread attention among researchers.[25−32] Compared with traditional electrodes with 2D metal current collectors, such as aluminum and copper foils, the continuous conductive network and high specific area of the 3D composite electrodes provide more attachment sites for electron transfer and effectively reduce the distance for ion transmission. The connected porous network can facilitate ion transport and increase the contact area between the electrolyte and active material. Also, binder-free 3D composite electrodes can effectively decrease the total mass of the batteries. Typical 3D composite electrodes include metal-based structures, such as nickel foams and aluminum nanorods,[25,26] and carbonaceous materials, such as graphene sponges,[29] CNT sponges,[30] and graphene/CNT composite sponges.[31] Compared with the metal-based 3D composite electrodes, the carbonaceous 3D composite electrodes have lower densities and better chemical stability, so that they can further increase the specific energy density of the cell and demonstrate higher electrochemical corrosion resistance in the electrolyte.[32]

Received: April 11, 2018
Accepted: May 21, 2018
Published: May 21, 2018

DOI: 10.1021/acsanm.8b00606
ACS Appl. Nano Mater. 2018, 1, 2997−3005

Herein, a simple and universal method is proposed to fabricate TMO composite electrodes based on macroporous and self-assembled CNT sponges that were reported recently by our group.[33] The CNT sponge has high "honeycomb-like" porosity, large specific surface area, and high electrical conductivity. TMO nanoparticles anchor onto the surface of the CNT skeleton by a facile freeze-drying method, followed by a calcination process. The structural characteristics of the CNT sponge lead to the accommodation of more active particles and a larger contact surface between the TMO nanoparticles and electrolyte. Meanwhile, it has been revealed that almost all kinds of TMOs with typical lattice structures, such as MnO_2 with a tetragonal structure, NiO with a rock-salt structure, Fe_2O_3 with a corundum structure, and Co_3O_4 with a spinal structure, can be made into composite electrodes with 3D CNT sponges. To the best of our knowledge, this is the first time that 3D CNT/TMO sponge electrodes are reported for LIBs through a one-step assembly process. The obtained CNT/TMO sponges exhibit excellent electrochemical properties, such as large reversible capacities, high cycling stability, and excellent rate performance. Notably, because of the unique macrostructure of the CNT sponge, the mass loading of TMOs can reach 5 mg cm^{-2}. Even at such high TMO loadings, the CNT/TMO electrodes still demonstrate excellent cycling and rate performances.

2. MATERIAL AND METHODS

2.1. Materials. Superaligned carbon nanotube (SACNT) arrays were prepared in a low-pressure chemical vapor system. The details of the synthesis procedure of SACNT arrays can be found in previous works.[34,35] Manganese nitrate tetrahydrate and manganese oxide were purchased from Alfa Aesar. Nickel nitrate hexahydrate, iron nitrate nonahydrate, and cobalt nitrate hexahydrate were purchased from Peking Reagent. All of the chemicals were analytical-grade reagents and were used as received.

2.2. Fabrication of the CNT/TMO Sponges. As shown in Figure 1, 50 mg of SACNTs were dispersed in 80 mL of deionized water, followed by tip sonication for 45 min. Subsequently, a certain amount of transition-metal nitrates (TMNs) was added to the SACNT dispersion with continuous magnetic stirring for 24 h. Then, the dispersion was dried to 20 mL at 80 °C in an oven and then underwent a freeze-drying procedure for about 24 h to obtain the CNT/TMN sponge. Oxidation of the CNT/TMN sponge was conducted in a muffle furnace at 250 °C for 5 h with a heating rate of 1 °C min^{-1}, and then a CNT/TMO sponge was achieved.

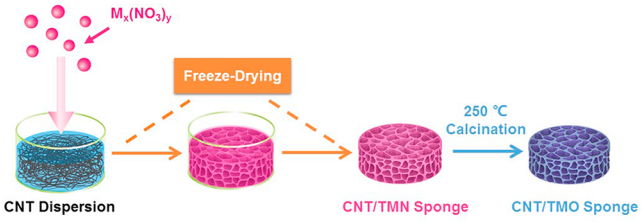

Figure 1. Schematic of the process for fabricating a CNT/TMO sponge by a freeze-drying and calcination process.

2.3. Characterization. The crystallinity and morphology of the CNT/TMO sponges were characterized by X-ray diffraction (XRD; Rigaku D/max-2500/PC), scanning electron microscopy (SEM; FEI Sirion 200, operated at 10 kV), and transmission electron microscopy (TEM; FEI Tecnai G2F20, operated at 200 kV). Thermogravimetric analysis (TGA) was conducted using a Pyris 1 thermogravimetric analyzer (PerkinElmer) at a heating rate of 10 °C min^{-1} in air.

2.4. Electrochemical Measurement. R2016-type coin batteries were assembled using the CNT/TMO sponges as the working electrode and lithium foil as the counter electrode in an argon-filled glovebox. The typical loading density of MnO_2 in the CNT/TMO sponge was ~5 mg cm^{-2}. The electrolyte was a 1.0 M $LiPF_6$ solution in an ethylene carbonate, dimethyl carbonate, and diethyl carbonate mixture with a volume ratio of 1:1:1, and the separator was a Celgard 2400 porous polypropylene membrane. For comparison, traditional MnO_2 electrodes were fabricated using commercial MnO_2 nanoparticles. Specifically, 50 wt % MnO_2 nanoparticles (~50 nm), 40 wt % Super P, and 10 wt % poly(vinylidene difluoride) were mixed and ground in a mortar for 30 min. The resulting slurry was cast on a copper foil, dried at 120 °C for 24 h under vacuum, and then cut into disks. The typical loading density of MnO_2 was ~1 mg cm^{-2}. The electrochemical properties of the CNT/TMO sponge and traditional MnO_2 electrodes were determined on a Land battery test system (Wuhan Land Electronic Co., China). Cyclic voltammetry (CV) and electrochemical impedance spectroscopy (EIS) were performed on a Princeton PARStat 2273 electrochemical station.

3. RESULTS AND DISCUSSION

During the freezing process, TMNs anchored onto the surface of CNTs because TMNs preferentially precipitated at the heterophase interfaces between CNTs and solutions. After sublimation of the ice phase and a calcination process, TMOs finally anchored onto the surface of CNTs. To ascertain the crystallinity and morphology of the CNT/TMO sponges, XRD, SEM, and TEM analyses were performed. The XRD patterns of the CNT/TMOs (Figure 2) were indexed as MnO_2 (PDF 53-0633), NiO (PDF 47-1049), Fe_2O_3 (PDF 33-0664), and Co_3O_4 (PDF 43-1003). The broad and weak peaks in these patterns indicated the presence of TMOs and their poor crystallinity in the corresponding composites after the calcination process. Additionally, no characteristic peak related to TMNs or other impurity was observed, which demonstrated complete thermal conversion from CNT/TMN sponges to CNT/TMO sponges. The peak at approximately 26° in all of the composites was assigned to the (002) plane of CNTs. X-ray photoelectron spectroscopy (XPS) spectra of the CNT/TMO sponges are shown in Figure S1. The spin-energy separations were 11.7 eV for MnO_2, 18 eV for NiO, 13.6 eV for Fe_2O_3, and 15.4 eV for Co_3O_4. These values indicated the dominance of Mn^{4+}, Ni^{2+}, and Fe^{3+} in the CNT/MnO_2, CNT/NiO, and CNT/Fe_2O_3 sponges and the Co^{2+} and Co^{3+} oxidation states in the CNT/Co_3O_4 sponge.[1,13,19,36]

To ensure high conductivity and structural stability of the CNT/TMO sponges, relatively large contents of CNTs were used. According to the TGA results, the contents of NiO, Fe_2O_3, Co_3O_4, and MnO_2 in the CNT/TMO sponges were 43%, 62%, 60%, and 44%, respectively (Figure 3a). The residues after the TGA tests were characterized by XRD and were still indexed as NiO, Fe_2O_3, and Co_3O_4, demonstrating no phase transition during the TGA tests. CNT was not observed in the residues (Figure 3b). However, for the CNT/MnO_2 sponge, the residue was indexed as Mn_2O_3 (Figure 3c; PDF 41-1442), which might be attributed to the reduction by CNTs. According to the XRD pattern and TGA result, the actual MnO_2 content was 51%.

The mechanical and electrical properties of the CNT/TMO sponges were characterized. The dimensions and weight of the CNT/MnO_2 sponge were 3.5 × 3.5 × 0.6 cm^3 and 100 mg, respectively. The free-standing CNT/MnO_2 sponge was highly flexible and recovered to its original state after pressing and release (Figure S2a–c). Compressive stress–strain curves of the CNT/MnO_2 sponge showed full recovery at 60% and 70%

DOI: 10.1021/acsanm.8b00606
ACS Appl. Nano Mater. 2018, 1, 2997–3005

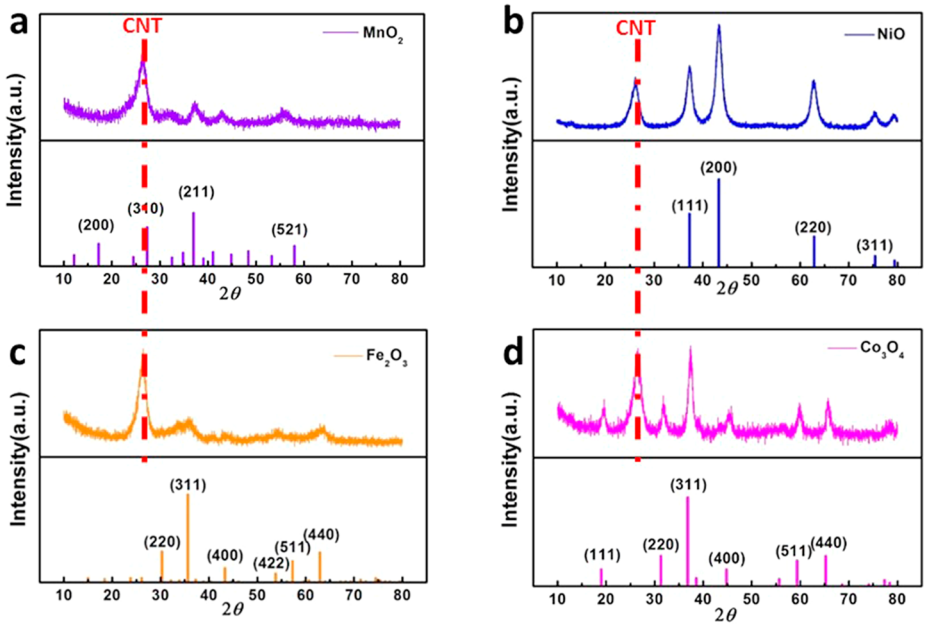

Figure 2. XRD patterns of the CNT/TMO sponges: (a) MnO_2; (b) NiO; (c) Fe_2O_3; (d) Co_3O_4.

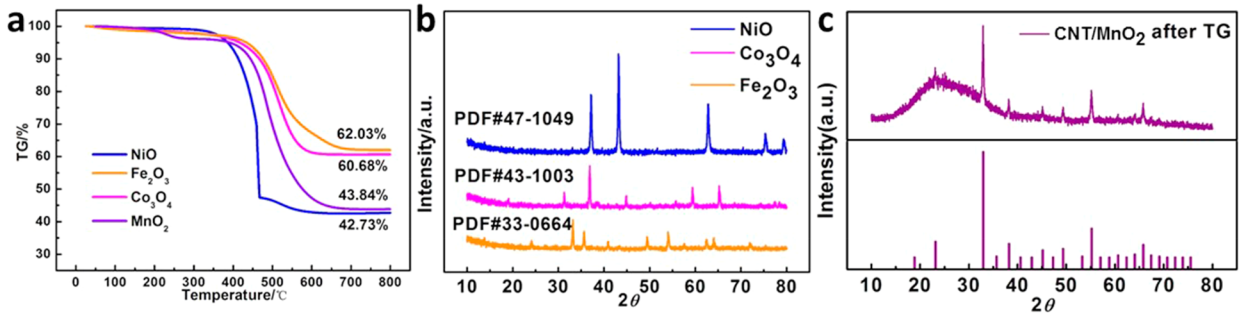

Figure 3. (a) TGA curves of the CNT/TMO sponges. XRD patterns of (b) NiO, Fe_2O_3, Co_3O_4, and (c) MnO_2 residues after TGA tests.

strains, suggesting its outstanding elastic resilience (Figure S2d). The conductivities of the CNT/MnO_2 sponge were 0.17 and 0.43 S m^{-1} at 60% and 70% strain, respectively (Figure S2e). Prior to battery assembly, the CNT/TMO sponges were pressed at a pressure of 10 MPa for 10 s, and their thicknesses decreased from 6 mm to around 100 μm (Figure S2f,g). After compression, the conductivities of the CNT/TMO electrodes increased significantly and reached 10^4 S m^{-1} (Table S1). The compressed CNT/TMO sponges still exhibited superior flexibility (Figure S2h). These results suggest that the CNT/TMO sponges have great potential in serving as flexible electrodes in supercapacitors and batteries.

Microstructures of the CNT/TMO sponges are shown in Figure 4a,e,i,m. All of the CNT/TMO sponges displayed a typically "honeycomb-like" hierarchical porous structure. As shown in Figure 4b,f,j, MnO_2, NiO, and Fe_2O_3 particles were deposited uniformly on the surface of the CNT skeletons without any visible agglomeration. For the CNT/Co_3O_4 sponge (Figure 4n), Co_3O_4 clusters were attached to the CNTs, which might be due to the relatively higher melting point and lower decomposition temperature of $Co(NO_3)_2 \cdot 6H_2O$. Therefore, the molten cobalt nitrates did not completely infiltrate into the CNT network and began to decompose during the calcination process. During the freeze-drying process, TMN molecules began to crystallize as the ice sublimed. By the calcination process, TMNs decomposed into TMOs. The size of the TMO particles was small and uniform. Especially, throughout the preparation procedure, exfoliation of the TMO particles was not observed. TEM images in Figure 4o demonstrated that the TMO particles were evenly dispersed in the CNT network, and the average particle sizes were below 30 nm. High-resolution TEM images in Figure 4d,h,l,p show that the TMO particles were partly crystalline. For MnO_2, the lattice spacings of 0.28 and 0.53 nm agreed well with the (101) and (200) planes. The (111) and (200) planes for NiO, the (012) and (104) planes with respect to Fe_2O_3, and the (111) and (220) planes for Co_3O_4 are shown in the TEM results.

Compared with traditional graphite electrodes, the TMO electrodes exhibited much higher specific capacities based on a conversion reaction mechanism: $M_xO_y + 2yLi \leftrightarrow xM + yLi_2O$. Typical TMOs could be classified as four different lattice structures: MO with a rock-salt structure, M_2O_3 with a corundum structure, M_3O_4 with a spinal structure, and MO_2 with a rutile structure. NiO, Fe_2O_3, Co_3O_4, and MnO_2 were chosen in this study. Among these TMOs, MnO_2 attracted more attention because of its diverse electrochemical properties resulting from various crystalline structures, being tetragonal in this work. To study the effect of the 3D CNT sponge on the electrochemical properties of the CNT/MnO_2 composite

DOI: 10.1021/acsanm.8b00606
ACS Appl. Nano Mater. 2018, 1, 2997−3005

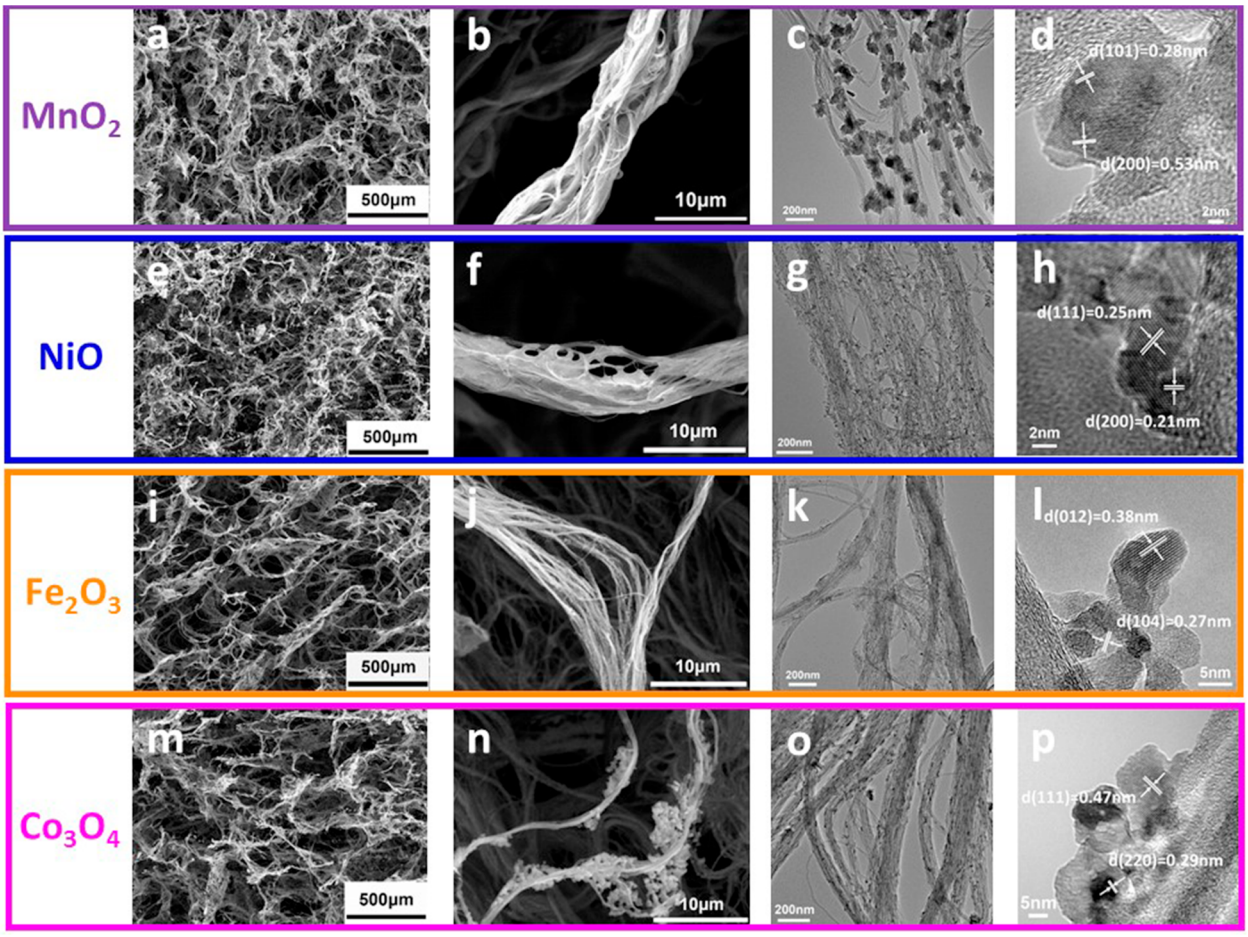

Figure 4. SEM and TEM images of the CNT/TMO sponges: (a–d) MnO_2; (e–h) NiO; (i–l) Fe_2O_3; (m–p) Co_3O_4.

electrode, the cycling performances of both traditional MnO_2 and CNT/MnO_2 electrodes were studied (Figure 5a). On the basis of the mass of MnO_2, the MnO_2 electrode delivered an initial discharge capacity of 1247 mA h g^{-1} with a relatively low Coulombic efficiency (47%) at 0.2 A g^{-1}, which could arouse from the generation of a solid electrolyte interface (SEI) film. Its reversible capacity was only 707 mA h g^{-1} after 100 cycles. In comparison, the CNT/MnO_2 electrode delivered a specific capacity of 1288 mA h g^{-1} after 100 cycles, which benefited from full contact with the electrolyte due to the high porosity of the 3D electrode microstructure. To identify the capacity contribution of CNTs in the composite electrodes, the cycling performance and voltage profiles of the pristine CNT sponge are shown in Figures 5b and S3. The discharge and charge specific capacities of the CNT sponge in the first cycle were 748 and 207 mA h g^{-1}, respectively. Eventually, the specific capacity stabilized at approximately 190 mA h g^{-1}. The reversible capacity based on the total mass of the CNT/MnO_2 electrode with 51 wt % MnO_2 was 657 mA h g^{-1}. The capacity contribution of the CNT sponge was 190 mA h g^{-1} × 49% = 93.1 mA h g^{-1}. By subtraction of the capacity of the CNT sponge, the actual specific capacity of MnO_2 in the CNT/MnO_2 electrode was 1105 mA h g^{-1}. Table 1 compares this study with the previous results of MnO_2-based electrodes in the past 2 years. The CNT/MnO_2 electrode in this study exhibited a relatively higher reversible capacity, which suggested the substantial advantages of the 3D CNT composite electrode microstructure.

Figure 5c shows the voltage profiles of the CNT/MnO_2 electrode after the 1st, 2nd, 10th, 25th, and 50th cycles. There were three plateaus at approximately 2.4, 1.1, and 0.9 V in the discharge profiles, which arose from the formation of Li_xMnO_2 (x = 1 and 2) and the SEI film.[2] Additionally, the 0.5 V plateau corresponded to the reduction of Li_xMnO_2 to metallic manganese. There were two plateaus at 1.3 and 2.2 V in the charge profiles, which were typical of the oxidation reactions of Mn^0 in two steps. From the second cycle onward, the discharge profiles were similar, indicating a stable cycling performance. For the charge profiles, the incline of the plateau was observed after the 10th, 25th, and 50th cycles, which indicated the thermodynamic effects of the amorphization process in electrodes.[4] Figure 5d shows a comparison of the rate performances of the CNT/MnO_2 and MnO_2 electrodes. The CNT/MnO_2 electrode delivered specific capacities of 1166, 1146, 1016, and 902 mA h g^{-1} at current densities of 0.2, 0.4, 1, and 2 A g^{-1}, respectively. In contrast, the MnO_2 electrode only delivered poorer specific capacities of 695, 467, 317, and 272 mA h g^{-1} at current densities of 0.2, 0.4, 1, and 2 A g^{-1}, respectively. Compared with the MnO_2 electrode, the CNT/MnO_2 electrode exhibited superior electrochemical properties.

To obtain further insight into the superior performance of the CNT/MnO_2 electrode compared with the MnO_2 electrodes, CV and EIS of both types of cells were also performed. CV profiles of both electrodes in the first and second cycles delivered two reduction peaks (0.65 and 2.1 V) and one oxidation peak (1.3 V), which can be described as the following

DOI: 10.1021/acsanm.8b00606
ACS Appl. Nano Mater. 2018, 1, 2997–3005

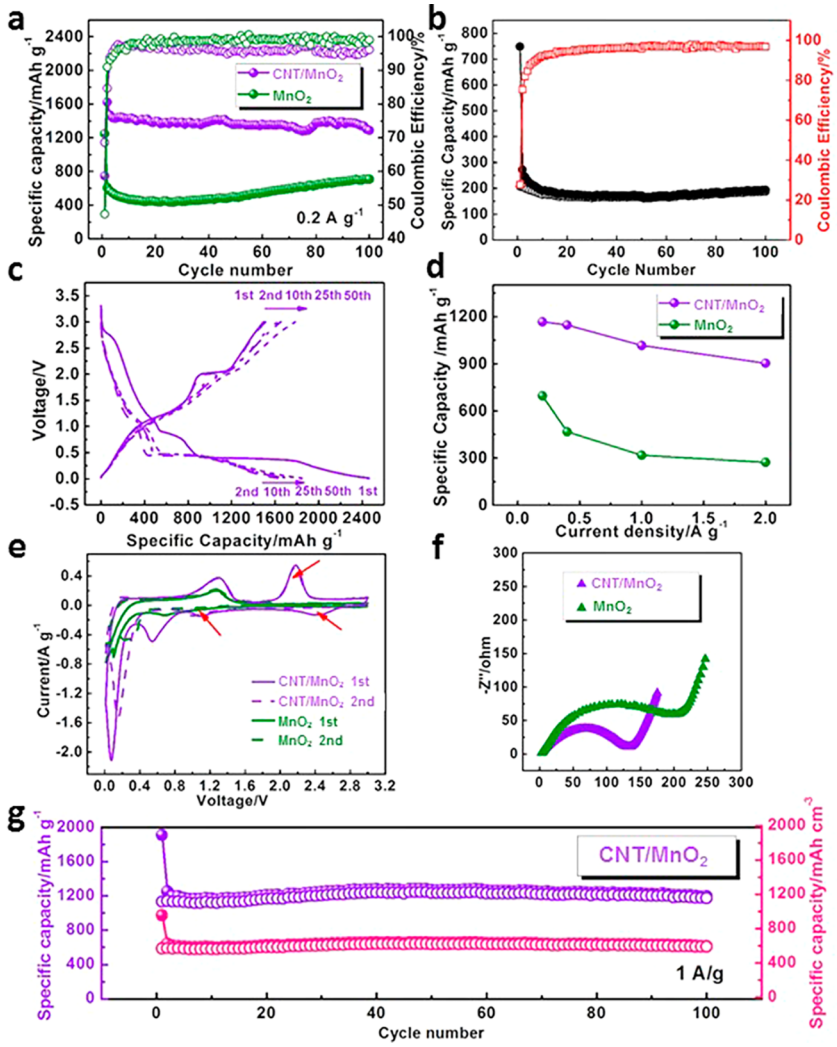

Figure 5. Electrochemical properties of the CNT/MnO_2 and MnO_2 electrodes: (a) Cycling performance at 0.2 A g^{-1}. (b) Cycling performance of the pure CNT sponge at 0.2 A g^{-1}. (c) Voltage profiles of the CNT/MnO_2 sponge in the 1st, 2nd, 10th, 25th, and 50th cycles at 0.2 A g^{-1}. (d) Rate performances at 0.2, 0.4, 1, 2, 4, 10, and 20 A g^{-1}. (e) Typical CV curves at a scan rate of 0.2 mV s^{-1}. (f) EIS curves in the frequency range from 100 kHz to 100 mHz. (g) Long cycling performance of the CNT/MnO_2 sponge at 1 A g^{-1}.

Table 1. Recent Reports on the Synthesis and Cycling Performance of MnO_2 Electrodes

sample	synthesis	current density (mA g^{-1})	capacity based on MnO_2/total mass (mA h g^{-1}) [cycle number]	ref
MnO_2@carbon sponge	solution method	200	1288/657 [100]	this study
MnO_2@N-CNT	hydrothermal reaction	100	1415/991 [100]	1
MnO_2/rGO nanocomposites	solution method	1000	1574/1062 [500]	2
hollow MnO_2 nanospheres	hydrothermal reaction	100	637/588 [60]	3
MnO_2	molten salt method	60	845/592 [50]	4
HPC-MnO_2	anodic electrochemical deposition	400	778/778 [200]	5
stacked MnO_2/rGO composites	solution method with microwave reactor	123	1100/880 [100]	6
α-MnO_2 nanotubes	hydrothermal reaction	800	618/494 [300]	7

reaction: $MnO_2 + 4Li^+ + 4e^- \leftrightarrow 2Li_2O + Mn$ [2] (Figure 5e). However, the reduction peak at 2.5 V in the first cycle, the reduction peak at 1.1 V, and the oxidation peak at 2.1 V observed in the CNT/MnO_2 electrode (indicated by the red arrows) were not present in the MnO_2 electrode. The loss of reversible capacity probably arose from the poor electrochemical kinetics in the MnO_2 electrode so that conversion reactions could not take place. Such CV results further confirmed the fast electrochemical kinetics of the CNT/MnO_2 electrode. As shown in Figure 5f, EIS spectra of the CNT/MnO_2 and MnO_2 electrodes were obtained in a frequency range from 100 kHz to 100 mHz. Nyquist plots of the EIS spectrum suggested that the CNT/MnO_2 electrode possessed a lower charge-transfer resistance according to the diameters of the semicircles, which was ascribed to the more effective conductive structures and their larger contact area with MnO_2. The cycling performance of the CNT/MnO_2 electrode at a current density of 1 A g^{-1} (close to 1 C) is shown in Figure 5g. The reversible capacity retained at approximately 1200 mA h g^{-1} after 100 cycles, which was close to the theoretical specific capacity of MnO_2 (~1230 mA h g^{-1}), and its corresponding volumetric specific capacity was 598 mA h cm^{-3}.

DOI: 10.1021/acsanm.8b00606
ACS Appl. Nano Mater. 2018, 1, 2997−3005

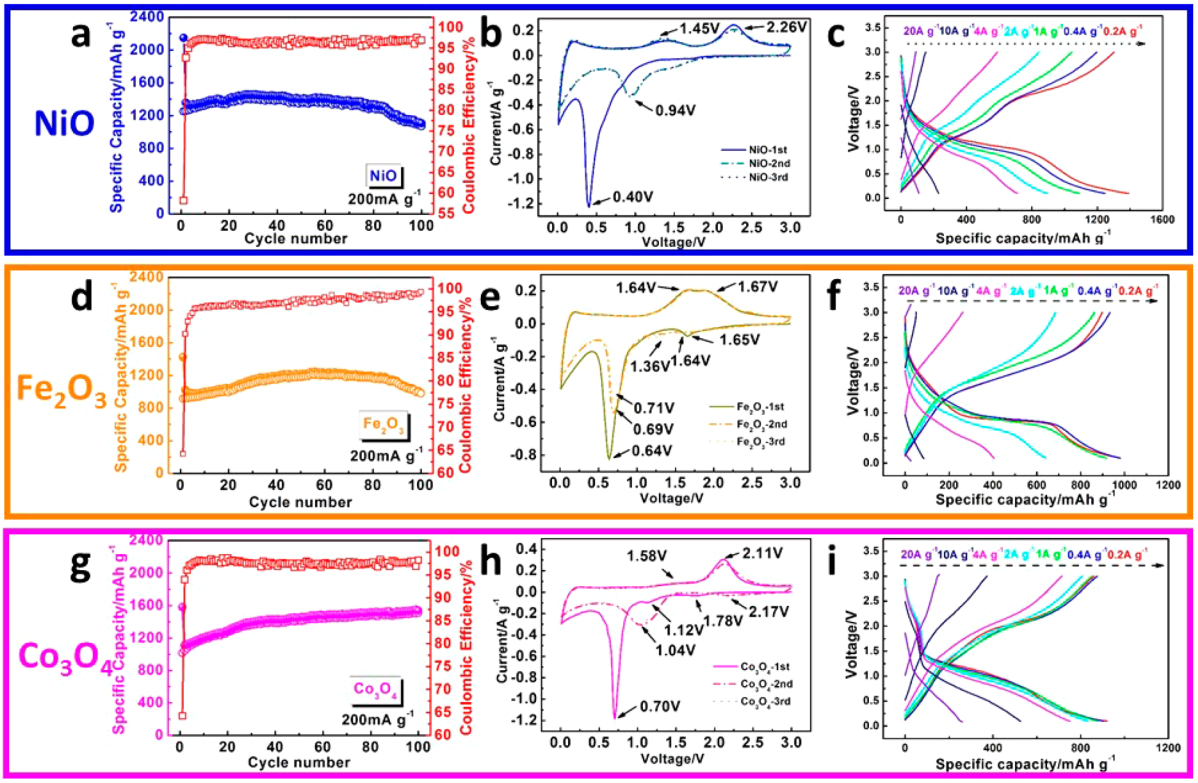

Figure 6. Cycling performances, CV curves in the first three cycles, and rate performances of the (a–c) CNT/NiO, (d–f) CNT/Fe_2O_3, and (g–i) CNT/Co_3O_4 electrodes.

The electrochemical properties of the CNT/NiO, CNT/Fe_2O_3, and CNT/Co_3O_4 composites were also studied. During cycling at 0.2 A g^{-1}, these electrodes exhibited an increase in the specific capacity (Figure 6). The discharge and charge specific capacities of the CNT/NiO electrode in the first cycle were 2146 and 1250 mA h g^{-1}, respectively, with a Coulombic efficiency of 58% (Figure 6a). The discharge capacity increased in the first 30 cycles because of the polymeric gel-like coatings resulting from kinetically activated electrolyte degradation[37] and decreased slightly for the subsequent 100 cycles. The Coulombic efficiency gradually increased and became stable at 97.5% because of lithium consumptions in the activation process and electrolyte decomposition.[12] The CV results are illustrated in Figure 6b. In the cathodic scan of the CNT/NiO electrode in the first cycle, the intense reduction peak at approximately 0.4 V was attributed to the formation of the SEI layer and the initial formation of Ni and Li_2O, according to the following reaction: $NiO + 2Li^+ + 2e^- \leftrightarrow Ni + Li_2O$.[12] In the following cycles, the peak became weaker and moved to 0.94 V, which resulted from textural modifications.[12] In the anodic scan, the weak peak at 1.45 V and the strong peak at 2.26 V were attributed to decomposition of the SEI layer and oxidation of metallic nickel, respectively.[11−13] At current densities of 0.2, 0.4, 1, 2, 4, 10, and 20 A g^{-1}, the specific discharge capacities of the CNT/NiO electrode were 1391, 1248, 1092, 895, 712, 229, and 109 mA h g^{-1}, respectively (Figure 6c).

The CNT/Fe_2O_3 electrode showed a discharge capacity of 1020 mA h g^{-1} in the second cycle, and the capacity increased to 1205 mA h g^{-1} after 65 cycles and decreased to 978 mA h g^{-1} after 100 cycles (Figure 6d). The cathodic peak at 0.64 V was attributed to a reduction from Fe^3 to Fe^0 and the formation of Li_2O and the SEI layer, corresponding to the following three lithiation steps: $Fe_2O_3 + xLi^+ + xe^- \leftrightarrow Li_xFe_2O_3 + (6 - x)Li^+ + (6 - x)e^- \leftrightarrow 2Fe + 3Li_2O$[16] (Figure 6e). The shoulder peaks at 1.36 and 1.64 V originated from the formation of $Li_xFe_2O_3$ (x = 1 and 2). The anodic peaks at 1.64 and 1.67 V reflected the processes from Fe^0 to Fe^2 and from Fe^2 to Fe^3, respectively. Similar to other CNT/TMO electrodes, the CNT/Fe_2O_3 electrode also demonstrated a good rate capability. The discharge capacities were 977, 980, 919, 643, 406, 85, and 26 mA h g^{-1} at the current densities of 0.2, 0.4, 1, 2, 4, 10, and 20 A g^{-1} (Figure 6f), respectively.

During cycling at 0.2 A g^{-1}, the discharge capacity of the CNT/Co_3O_4 electrode dropped to 1110 mA h g^{-1} in the second cycle and subsequently increased to 1536 mA h g^{-1} after 100 cycles (Figure 6g). The tendency of the capacity to increase in the CNT/Co_3O_4 electrode might result from activation of the electrode materials and the reversible growth of the polymeric gel-like film.[1,4,37] The reduction peaks at 1.12 and 0.7 V were attributed to the formation of $Li_xCo_3O_4$ and metallic cobalt, respectively. The oxidation peaks at 1.58 and 2.11 V were associated with the oxidation of metallic cobalt into various cobalt oxides (Figure 6h). Additionally, for the cathodic scan, the reduction peaks shifted to 1.04 and 2.17 V after the second cycle, and the CV curves in the subsequent cycles were almost identical, which suggested excellent reversibility and cycling stability of the CNT/Co_3O_4 electrode. The electrochemical reaction mechanism of Co_3O_4 with Li can be expressed as $Co_3O_4 + 8Li^+ + 8e^- \leftrightarrow 4Li_2O + 3Co$.[17] Concerning the rate performance, the electrodes delivered a discharge capacity of 920 mA h g^{-1} at 0.2 A g^{-1}, 904 mA h g^{-1} at 0.4 A g^{-1}, 878 mA h g^{-1} at 1 A g^{-1}, 834 mA h g^{-1} at 2 A g^{-1}, 751 mA h g^{-1} at 4 A g^{-1}, 527 mA h g^{-1} at 10 A g^{-1}, and 261 mA h g^{-1} at 20 A g^{-1}. Notably, the CNT/TMO electrode

DOI: 10.1021/acsanm.8b00606
ACS Appl. Nano Mater. 2018, 1, 2997−3005

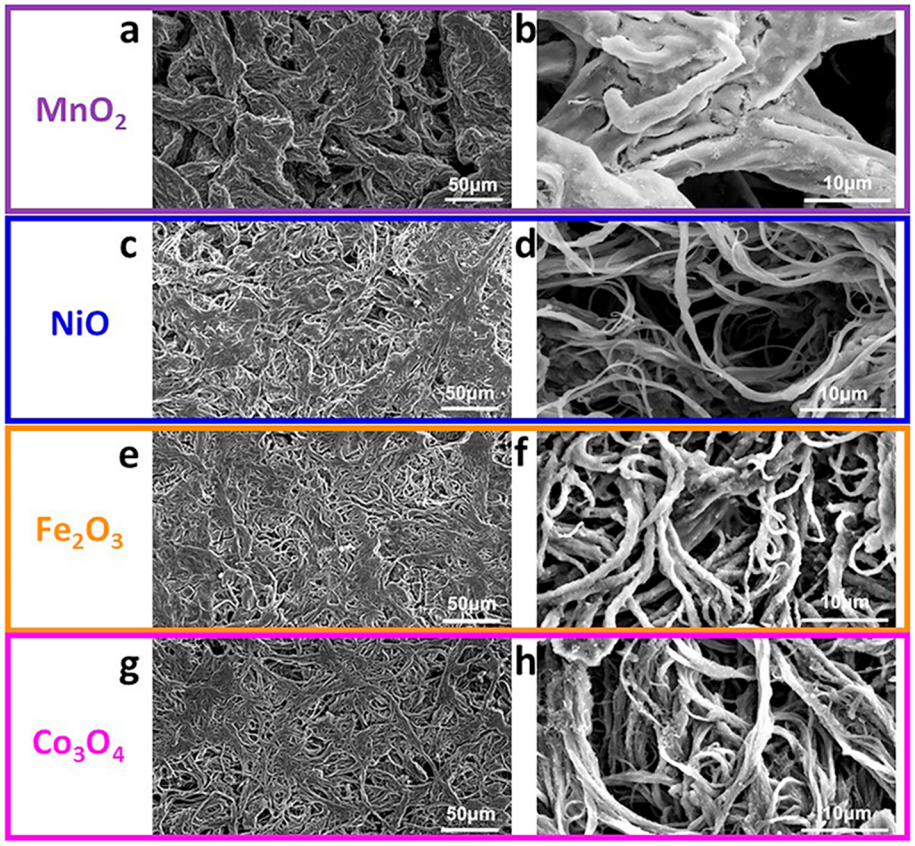

Figure 7. SEM images of the CNT/TMO electrodes after 50 cycles: (a and b) MnO_2; (c and d) NiO; (e and f) Fe_2O_3; (g and h) Co_3O_4.

exhibited a good rate performance at current densities as high as 10 A g^{-1} (Figure 6i).

SEM images of the CNT/TMO electrodes after 50 cycles are shown in Figure 7. Uniform polymeric layers were coated on the surface of CNTs, which were SEI layers generated during the galvanostatic discharge and charge processes. There was no obvious crack or structural change in the CNT network, indicating the excellent structural stability and robustness of the 3D CNT composite electrodes for use in LIBs. Notably, compared with the other three electrodes, the CNT/MnO_2 electrode exhibited severer agglomeration, showing poorer distribution of the larger MnO_2 particles (Figure 4c). The discharge product Li_2O was electrochemically irreversible, and the other discharge product Mn^0 played a catalytic role in the decomposition of Li_2O in the charging process.[38] The large particle size of MnO_2 might severely limit the reversibility of the electrochemical reaction. Morever, the severe volumetric expansion during cycling led to the loss of active materials by forming the SEI layer. Therefore, the Coulombic efficiency of the CNT/MnO_2 electrode after 100 cycles was lower than the other three CNT/TMO electrodes. A systematic comparison of the electrochemical performances of different CNT/TMO electrodes is shown in Table S2. The specific capacities of the CNT/NiO, CNT/Fe_2O_3, CNT/Co_3O_4, and CNT/MnO_2 electrodes were 844, 687, 808, and 902 mA h g^{-1} at 2 A g^{-1}. Notably, even at 4 A g^{-1}, CNT/NiO still delivered a specific capacity of 712 mA h g^{-1}, which was almost equal to its theoretical value (718 mA h g^{-1}). In comparison, most graphene/TMO sponges reported in the literature did not exhibit good rate performance, especially at current densities higher than 2 A g^{-1} in thick electrodes.[39−44] Besides, the reversible capacities of the CNT/NiO, CNT/Co_3O_4, and CNT/MnO_2 electrodes were 1104, 1536, and 1287 mA h g^{-1} after 100 cycles at 0.2 A g^{-1}, higher than their theoretical values. The excess capacity might originate from the extra lithium storage at TMO surfaces. XPS C 1s spectra of the CNTs and CNT/TMO electrodes are shown in Figure S4. The C−O contents in the CNTs and CNT/TMO electrodes were 3.8, 12.2, 12.5, 12.6, and 12.3%. The larger C−O contents in the CNT/TMO electrodes might be ascribed to the formation of the C−O−TM bonds at the TMO and CNT interface during the calcination process. Lithium storage at the reconstructed TMO surfaces contributed to the excess capacities in the CNT/TMO electrodes.[45,46]

All of the CNT/TMO electrodes exhibited excellent electrochemical properties including high reversible capacities and excellent cycling/rate performances. The outstanding properties were ascribed to the unique characteristics of 3D and porous CNT/TMO composite electrode microstructures: (i) high porosity provided a large contact area between the TMO nanoparticles and electrolyte and more space to accommodate any volumetric expansion; (ii) high specific surface area offered more attachment sites to anchor TMO nanoparticles and more contact areas between the 3D carbon sponges and TMO nanoparticles to improve the reaction activity; (iii) the CNT network provided a large number of conductive pathways to achieve fast electrochemical reaction kinetics; (iv) the self-assembly structures eliminated the need for polymeric binders so that the conductivities of the electrodes will not be compromised. Owing to all of these advantages, the electrochemical performances of the CNT/

DOI: 10.1021/acsanm.8b00606
ACS Appl. Nano Mater. 2018, 1, 2997−3005

TMO electrodes have been significantly improved compared with traditional TMO electrodes.

4. CONCLUSIONS

In summary, a simple and universal strategy is proposed to prepare binder-free and self-assembled CNT/TMO electrodes based on 3D CNT sponges. The CNT/TMO composite electrodes possessed a "honeycomb-like" porous structure with CNT skeletons, and the TMO nanoparticles were anchored onto the skeletons by a freeze-drying and calcination procedure. Compared with traditional TMO electrodes, the CNT/TMO electrodes exhibited high reversible capacity, stable cycling performance, and excellent rate capability. These excellent electrochemical properties all benefited from the unique characteristics of the 3D CNT/TMO composite electrode microstructures: high porosity, large specific surface area, and continuous conductive network. Furthermore, this processing strategy and the unique 3D structures can be easily applied to other material systems, demonstrating their further applications in lithium−sulfur batteries, supercapacitors, catalysts in fuel cells, and sensors.

■ ASSOCIATED CONTENT

Supporting Information

The Supporting Information is available free of charge on the ACS Publications website at DOI: 10.1021/acsanm.8b00606.

XPS spectra of Mn 2p, Ni 2p, Fe 2p, and Co 2p in the CNT/TMO sponges and their corresponding C 1s XPS spectra, photographs of a CNT/MnO_2 sponge before and after compression, stress−strain curves, and current−time curves of a CNT/MnO_2 sponge, voltage profiles of a pristine CNT sponge at a current density of 0.2 A g^{-1}, electrical conductivities of CNT and CNT/TMO sponges, and a comparison of the electrochemical performances (PDF)

■ AUTHOR INFORMATION

Corresponding Author

*E-mail: jpwang@tsinghua.edu.cn.

ORCID

Qunqing Li: 0000-0001-9565-0855

Jiaping Wang: 0000-0002-8300-4992

Notes

The authors declare no competing financial interest.

■ ACKNOWLEDGMENTS

This work was supported by the National Science Foundation of China (Grant 51472141) and the National Key Research and Development Program of China (Grant 2017YFA0205800).

■ REFERENCES

(1) Yue, J.; Gu, X.; Jiang, X. L.; Chen, L.; Wang, N. N.; Yang, J.; Ma, X. J. Coaxial Manganese Dioxide@N-doped Carbon Nanotubes as Superior Anodes for Lithium Ion Batteries. *Electrochim. Acta* **2015**, *182*, 676−681.

(2) Lee, S. W.; Lee, C. W.; Yoon, S. B.; Kim, M. S.; Jeong, J. H.; Nam, K. W.; Roh, K. C.; Kim, K. B. Superior Electrochemical Properties of Manganese Dioxide/Reduced Graphene Oxide Nanocomposites as Anode Materials for High Performance Lithium Ion Batteries. *J. Power Sources* **2016**, *312*, 207−215.

(3) Yue, J.; Gu, X.; Chen, L.; Wang, N. N.; Jiang, X. L.; Xu, H. Y.; Yang, J.; Qian, Y. T. General Synthesis Of Hollow Mno_2, Mn_3O_4 and Mno Nanospheres as Superior Anode Materials for Lithium Ion Batteries. *J. Mater. Chem. A* **2014**, *2*, 17421−17426.

(4) Nithyadharseni, P.; Reddy, M. V.; Fanny, H.; Adams, S.; Chowdari, B. V. R. Facile One Pot Synthesis and Li-cycling Properties of MnO_2. *RSC Adv.* **2015**, *5*, 60552−60561.

(5) Liu, S. K.; Liu, X. S.; Zhao, J. P.; Tong, Z. Q.; Wang, J.; Ma, X. X.; Chi, C. X.; Su, D. P.; Liu, X. X.; Li, Y. Three Dimensional Hierarchically Porous Crystalline MnO_2 Structure Design for a High Rate Performance Lithium-ion Battery Anode. *RSC Adv.* **2016**, *6*, 85222−85229.

(6) Kim, S. J.; Yun, Y. J.; Kim, K. W.; Chae, C. J.; Jeong, S. H.; Kang, Y. K.; Choi, S. Y.; Lee, S. S.; Choi, S. H. Superior Lithium Storage Performance using Sequentially Stacked MnO_2/Reduced Graphene Oxide Composite Electrodes. *ChemSusChem* **2015**, *8*, 1484−1491.

(7) Li, L. H.; Nan, C. Y.; Lu, J.; Peng, Q.; Li, Y. D. α-MnO_2 Nanotubes: High Surface Area and Enhanced Lithium Battery Properties. *Chem. Commun.* **2012**, *48*, 6945−6947.

(8) Liu, D. W.; Zhang, Q. F.; Xiao, P.; Garcia, B. B.; Guo, Q.; Champion, R.; Cao, G. Z. Hydrous Manganese Dioxide Nanowall Arrays Growth and Their Li+ Ions Intercalation Electrochemical Properties. *Chem. Mater.* **2008**, *20*, 1376−1380.

(9) Yu, A. P.; Park, H. W.; Davies, A.; Higgins, D. C.; Chen, Z. W.; Xiao, X. C. Free-Standing Layer-By-Layer Hybrid Thin Film of Graphene-MnO_2 Nanotube as Anode for Lithium Ion Batteries. *J. Phys. Chem. Lett.* **2011**, *2*, 1855−1860.

(10) Reddy, A. L. M.; Shaijumon, M. M.; Gowda, S. R.; Ajayan, P. M. Coaxial MnO_2/Carbon Nanotube Array Electrodes for High-Performance Lithium Batteries. *Nano Lett.* **2009**, *9*, 1002−1006.

(11) Lin, F. N.; Wang, H.; Wang, G. Facile Synthesis of Hollow Polyhedral (Cubic, Octahedral and Dodecahedral) NiO with Enhanced Lithium Storage Capabilities. Electrochim. *Electrochim. Acta* **2016**, *211*, 207−216.

(12) Pang, H. C.; Guan, B. Q.; Sun, W. W.; Wang, Y. Metal-Organic-Frameworks Derivation of Mesoporous NiO Nanorod for High-Performance Lithium Ion Batteries. Electrochim. *Electrochim. Acta* **2016**, *213*, 351−357.

(13) Liu, C.; Li, C. L.; Ahmed, K.; Mutlu, Z.; Ozkan, C. S.; Ozkan, M. Template Free and Binderless NiO Nanowire Foam for Li-ion Battery Anodes with Long Cycle Life and Ultrahigh Rate Capability. *Sci. Rep.* **2016**, *6*, 29183.

(14) Lee, K. S.; Park, S.; Lee, W.; Yoon, Y. S. Hollow Nanobarrels of α-Fe_2O_3 on Reduced Graphene Oxide as High Performance Anode for Lithium-Ion Batteries. *ACS Appl. Mater. Interfaces* **2016**, *8*, 2027−2034.

(15) Qiu, J.; Li, M. J.; Zhao, Y.; Kong, Q. S.; Li, X. G.; Li, C. X. Scalable Synthesis of Nanometric α-Fe_2O_3 within Interconnected Carbon Shells from Pyrolytic Alginate Chelates for Lithium Storage. *RSC Adv.* **2016**, *6*, 7961−7969.

(16) Kong, D. Z.; Cheng, C. W.; Wang, Y.; Liu, B.; Huang, Z. X.; Yang, H. Y. Seed-assisted Growth of α-Fe_2O_3 Nanorod Arrays on Reduced Graphene Oxide: A Superior Anode for High Performance Li-Ion and Na-Ion Batteries. *J. Mater. Chem. A* **2016**, *4*, 11800−11811.

(17) Zhao, Y.; Li, Y.; Ma, C. L.; Shao, Z. P. Micro-/Nano-Structured Hybrid of Exfoliated Graphite and Co_3O_4 Nanoparticles as High-Performance Anode Material for Li-Ion Batteries. Electrochim. *Electrochim. Acta* **2016**, *213*, 98−106.

(18) Wang, X.; Zhou, B.; Guo, J.; Zhang, W. P.; Guo, X. H. Selective Crystal Facets Exposing of Dumbbell-Like Co_3O_4 towards High Performances Anode Materials in s. *Mater. Res. Bull.* **2016**, *83*, 414−422.

(19) Wu, Z. S.; Ren, W. C.; Wen, L.; Gao, L. B.; Zhao, J. P.; Chen, Z. P.; Zhou, G. M.; Li, F.; Cheng, H. M. Graphene Anchored with Co_3O_4 Nanoparticles as Anode of Lithium Ion Batteries with Enhanced Reversible Capacity and Cyclic Performance. *ACS Nano* **2010**, *4*, 3187−3194.

(20) Wang, Z. Y.; Zhou, L.; Lou, X. W. D. Metal Oxide Hollow Nanostructures for Lithium-ion Batteries. *Adv. Mater.* **2012**, *24*, 1903−1911.

DOI: 10.1021/acsanm.8b00606
ACS Appl. Nano Mater. 2018, 1, 2997−3005

(21) Lu, Z. P.; Wang, H.; Zhou, T.; Ma, C.; Yin, F.; Jiang, X. F.; Yang, G. $CoCO_3$ Micrometer Particles Stabilized by Carbon Nanofibers Networks as Composite Electrode for Enhanced Rate and Cyclic Performance of Lithium-Ion Batteries. *Electrochim. Acta* **2018**, *270*, 22−29.
(22) Jiang, J. L.; Ma, C.; Yang, Y. B.; Ding, J. J.; Ji, H. M.; Shi, S. J.; Yang, G. Synergetic Interface Between NiO/Ni_3S_2 Nanosheets and Carbon Nanofiber as Binder-Free Anode for Highly Reversible Lithium Storage. *Appl. Surf. Sci.* **2018**, *441*, 232−238.
(23) Wang, T.; Li, H. G.; Shi, S. J.; Liu, T.; Yang, G.; Chao, Y. M.; Yin, F. 2D Film of Carbon Nanofibers Elastically Astricted MnO Microparticles: A Flexible Binder-Free Anode for Highly Reversible Lithium Ion Storage. *Small* **2017**, *13*, 1604182.
(24) Zhu, J. X.; Zhu, T.; Zhou, X. Z.; Zhang, Y. Y.; Lou, X. W.; Chen, X. D.; Zhang, H.; Hng, H. H.; Yan, Q. Y. Facile Synthesis of Metal Oxide/Reduced Graphene Oxide Hybrids with High Lithium Storage Capacity and Stable Cyclability. *Nanoscale* **2011**, *3*, 1084−1089.
(25) Wang, C. D.; Xu, J. L.; Yuen, M. F.; Zhang, J.; Li, Y. Y.; Chen, X. F.; Zhang, W. J. Hierarchical Composite Electrodes of Nickel Oxide Nanoflake 3D Graphene for High-Performance Pseudocapacitors. *Adv. Funct. Mater.* **2014**, *24*, 6372−6380.
(26) Shaijumon, M. M.; Perre, E.; Daffos, B.; Taberna, P. L.; Tarascon, J. M.; Simon, P. Nanoarchitectured 3D Cathodes for Li-Ion Microbatteries. *Adv. Mater.* **2010**, *22*, 4978−4981.
(27) Liao, J. Y.; Higgins, D.; Lui, G.; Chabot, V.; Xiao, X. C.; Chen, Z. W. Multifunctional TiO_2−C/MnO_2 Core−Double-Shell Nanowire Arrays as High-Performance 3D Electrodes for Lithium Ion Batteries. *Nano Lett.* **2013**, *13*, 5467−5473.
(28) Chabi, S.; Peng, C.; Hu, D.; Zhu, Y. Q. Ideal Three-Dimensional Electrode Structures for Electrochemical Energy Storage. *Adv. Mater.* **2014**, *26*, 2440−2445.
(29) He, J. R.; Chen, Y. F.; Lv, W. Q.; Wen, K. C.; Li, P. J.; Qi, F.; Wang, Z. G.; Zhang, W. L.; Li, Y. R.; Qin, W.; He, W. D. Highly-Flexible 3D Li_2S/Graphene Cathode for High-Performance Lithium Sulfur Batteries. *J. Power Sources* **2016**, *327*, 474−480.
(30) Lin, Z. Q.; Zeng, Z. P.; Gui, X. C.; Tang, Z. K.; Zou, M. C.; Cao, A. Y. Carbon Nanotube Sponges, Aerogels, and Hierarchical Composites: Synthesis, Properties, and Energy Applications. *Adv. Energy Mater.* **2016**, *6*, 1600554.
(31) Liu, Y.; Cai, X. Y.; Shi, W. D. Free-Standing Graphene/Carbon Nanotubes/Cuo Aerogel Paper Anode for Lithium Ion Batteries. *Mater. Lett.* **2016**, *172*, 72−75.
(32) Peng, H. J.; Xu, W. T.; Zhu, L.; Wang, D. W.; Huang, J. Q.; Cheng, X. B.; Yuan, Z.; Wei, F.; Zhang, Q. 3D Carbonaceous Current Collectors: The Origin of Enhanced Cycling Stability for High-Sulfur-Loading Lithium−Sulfur Batteries. *Adv. Funct. Mater.* **2016**, *26*, 6351−6358.
(33) Luo, S.; Luo, Y. F.; Wu, H. C.; Li, M. Y.; Yan, L. J.; Jiang, K. L.; Liu, L.; Li, Q. Q.; Fan, S. S.; Wang, J. P. Self-assembly of 3D Carbon Nanotube Sponges: A Simple and Controllable Way to Build Macroscopic and Ultralight Porous Architectures. *Adv. Mater.* **2017**, *29*, 1603549.
(34) Zhang, X. B.; Jiang, K. J.; Feng, C.; Liu, P.; Zhang, L. N.; Kong, J.; Zhang, T. H.; Li, Q. Q.; Fan, S. S. Spinning and Processing Continuous Yarns from 4-Inch Wafer Scale Super-Aligned Carbon Nanotube Arrays. *Adv. Mater.* **2006**, *18*, 1505−1510.
(35) Liu, K.; Sun, Y. H.; Chen, L.; Feng, C.; Feng, X. F.; Jiang, K. L.; Zhao, Y. G.; Fan, S. S. Controlled Growth of Super-Aligned Carbon Nanotube Arrays for Spinning Continuous Unidirectional Sheets with Tunable Physical Properties. *Nano Lett.* **2008**, *8*, 700−705.
(36) Bak, B. M.; Kim, S. K.; Park, H. S. Binder-Free, Self-Standing Films of Iron Oxide Nanoparticles Deposited in Ionic Liquid Functionalized Carbon Nanotubes for Lithium-Ion Battery Anodes. *Mater. Chem. Phys.* **2014**, *144*, 396−401.
(37) Grugeon, S.; Laruelle, S.; Dupont, L.; Tarascon, J. M. An Update on The Reactivity of Nanoparticles Co-Based Compounds towards Li. *Solid State Sci.* **2003**, *5*, 895−904.
(38) Kang, Y. M.; Song, M. S.; Kim, J. H.; Kim, H. S.; Park, M. S.; Lee, J. Y.; Liu, H. K.; Dou, S. X. A Study on the Charge-Discharge Mechanism of Co_3O_4 as An Anode for the Li Ion Secondary Battery. Electrochim. *Electrochim. Acta* **2005**, *50*, 3667−3673.
(39) Wang, J.; Fang, F.; Yuan, T.; Yang, J. H.; Chen, L.; Yao, C.; Zheng, S. Y.; Sun, D. L. Three-Dimensional Graphene/Single-Walled Carbon Nanotube Aerogel Anchored with SnO_2 Nanoparticles for High Performance Lithium Storage. *ACS Appl. Mater. Interfaces* **2017**, *9*, 3544−3553.
(40) Liu, H.; Jia, M. Q.; Zhu, Q. Z.; Cao, B.; Chen, R. J.; Wang, Y.; Wu, F.; Xu, B. 3D-0D Graphene-Fe_3O_4 Quantum Dot Hybrids as High-Performance Anode Materials for Sodium-Ion Batteries. *ACS Appl. Mater. Interfaces* **2016**, *8*, 26878−26885.
(41) Jiang, T. C.; Bu, F. X.; Feng, X. X.; Shakir, I.; Hao, G. L.; Xu, Y. X. Porous Fe_2O_3 Nanoframeworks Encapsulated within Three-Dimensional Graphene as High-Performance Flexible Anode for Lithium-Ion Battery. *ACS Nano* **2017**, *11*, 5140−5147.
(42) Ding, C. Y.; Zhou, W. W.; Wang, X. Y.; Shi, B.; Wang, D.; Zhou, P. Y.; Wen, G. W. Hybrid Aerogel-Derived Carbon/Porous Reduced Graphene Oxide Dual-Functionalized NiO for High-Performance Lithium Storage. *Chem. Eng. J.* **2018**, *332*, 479−485.
(43) Sun, L. N.; Deng, Q. W.; Li, Y. L.; Mi, H. W.; Wang, S. H.; Deng, L. B.; Ren, X. Z.; Zhang, P. X. CoO-Co_3O_4 Heterostructure Nanoribbon/RGO Sandwich-Like Composites as Anode Materials for High Performance Lithium-Ion Batteries. *Electrochim. Acta* **2017**, *241*, 252−260.
(44) Sun, H. T.; Mei, L.; Liang, J. F.; Zhao, Z. P.; Lee, C.; Fei, H. L.; Ding, M. N.; Lau, J.; Li, M. F.; Wang, C.; Xu, X.; Hao, G. L.; Papandrea, B.; Shakir, I.; Dunn, B.; Huang, Y.; Duan, X. F. Three-Dimensional Holey-Graphene/ Niobia Composite Architectures for Ultrahigh-Rate Energy Storage. *Science* **2017**, *356*, 599−604.
(45) Duan, Y. D.; Zhang, B. K.; Zheng, J. X.; Hu, J. T.; Wen, J. G.; Miller, D. J.; Yan, P. F.; Liu, T. C.; Guo, H.; Li, W.; Song, X. H.; Zhuo, Z. Q.; Liu, C. K.; Tang, H. T.; Tan, R.; Chen, Z. H.; Ren, Y.; Lin, Y.; Yang, W. L.; Wang, C. M.; Wang, L. W.; Lu, J.; Amine, K.; Pan, F. Excess Li-Ion Storage on Reconstructed Surfaces of Nanocrystals to Boost Battery Performance. *Nano Lett.* **2017**, *17*, 6018−6026.
(46) Zhou, G. M.; Wang, D. W.; Yin, L. C.; Li, N.; Li, F.; Cheng, H. M. Oxygen Bridges Between NiO Nanosheets and Graphene for Improvement of Lithium Storage. *ACS Nano* **2012**, *6*, 3214−3223.

DOI: 10.1021/acsanm.8b00606
ACS Appl. Nano Mater. 2018, 1, 2997−3005